




Coupling between vortex flow and whisker sensor in cylinder wakes with time-varying streamwise gaps

Pengyao Gong ^{*}, Dhanush Bhamitipadi Suresh [†], and Yaqing Jin [‡]

Department of Mechanical Engineering, University of Texas at Dallas, Richardson, Texas 75080, USA



(Received 14 October 2022; accepted 7 February 2023; published 22 March 2023)

The flow-induced vibration of a whisker in the wake of a movable circular cylinder with time-varying streamwise gaps was experimentally investigated to understand how whiskers detect the variation of upstream target's swimming status. A time-resolved particle image velocimetry was used to characterize the vortex flow dynamics and vibrations of whisker across various initial gaps and gap growth rates. Results showed that despite the time-varying gaps, the evolution of vortex flow and whisker dynamics remained overall synchronized. Due to the nonlinear decaying rate of vortex strength along streamwise direction, the vibrations of whisker sensor were more sensitive to gap growth rates with smaller initial gaps. However, the sensitivity of whisker (i.e., the decaying rate of whisker vibration intensity over unit time) to gap growth rates gradually decreased when such growth rate became sufficiently high, regardless of initial gaps. Using a physical model based on the balance between whisker inertial force, system damping, restoring force, and flow loading with time-varying magnitudes, we well described the response of whisker sensor in the cylinder wake flow; the model revealed that the reduction of whisker's sensitivity under high gap growth rate was attributed to the sufficiently strong vortices initiated by the fast movement of upstream cylinder, which compensated the influence of vortex strength decay due to the growth of gap. In addition to cases with whisker vibrating in the wake centerline, our complementary measurements with the whisker in the cylinder edge highlighted the time-varying equilibrium vibration positions of whisker sensor due to the "wake-stiffness" effect.

DOI: [10.1103/PhysRevFluids.8.034701](https://doi.org/10.1103/PhysRevFluids.8.034701)

I. INTRODUCTION

Aquatic animals such as harbor seals have presented their extraordinary abilities in hunting their prey by utilizing the vibration signals from their whiskers [1–4]. When seals are approaching the upstream prey, their whiskers can sense the hydrodynamic information induced by the swimming prey across large gap distances [5]. This capability allows seals to hunt in turbid seawater and other complex flow environments where their auditory and visual sensing are limited.

The phenomenon of wake-induced vibrations (WIV) plays a key role in the flow sensing of seals with their whiskers. Different from the vortex-induced vibration (VIV) induced by the unsteady Kármán vortex shedding from its own body [6], the WIV usually occurs with multiple bluff bodies located close to each other, where the vibration of the downstream object is highly modulated by the wake characteristics from the upstream counterparts. To well understand the mechanisms of WIV, during the last decades, extensive efforts have focused on the interference of two fixed circular cylinders in cross-flow with various arrangements [7–9], where the velocity deficit, vortex

^{*}Pengyao.Gong@UTDallas.edu

[†]dhanush.bhamitipadisuresh@utdallas.edu

[‡]Yaqing.Jin@UTDallas.edu

shedding frequencies and flow loads of the downstream one are proved to be highly influenced by the gap distance and incidence angle between the two cylinders. While the maximum oscillation amplitude of VIV occurs with the vortex shedding frequency approaching the natural frequency of the structure, the WIV was reported to present a build-up of amplitude persisting to the increase of incoming flow velocity [10–12]. A systematic experimental investigation by Assi *et al.* [12] revealed that WIV of the downstream cylinder is excited by the unsteady vortex shedding from the upstream counterpart; for cylinders placed in a shear-flow environment without vortex shedding, their vibration modes returned to VIV. It is worth pointing out that the gap distance between the two cylinders plays an important role in defining the dynamic modes of the downstream cylinder vibrations [13]. For two cylinders placed in tandem with small gaps ($S_x/d_c \leq 4$, where S_x is the gap distance and d_c represents the cylinder diameter), the downstream one may present mixed patterns with VIV and WIV [14]. Distinct WIV of downstream cylinder occurs with the $4 \leq S_x/d_c \leq 8$ [15], while its behavior gradually converged to VIV with further growth of S_x/d_c due to the decaying of vortex shedding from the upstream cylinder [12]. Following work by Assi [16] showed that regardless of diameter ratios between two tandem cylinders, the frequency response of the downstream one presented similar behaviors. In addition to cases with two cylinders aligned in flow, Hover and Triantafyllou [17] investigated the vibration of the downstream cylinder located one diameter offset from the wake center-line of the upstream one; results indicated that at the same S_x/d_c , the offset cases presented lower vibration amplitude compared to the aligned counterparts.

Despite the extensive efforts on WIV of circular cylinders, the geometries of whiskers of seals and other animals usually present unique patterns. Hanke *et al.* [18], Ginter *et al.* [19] reported that the cross-section of whiskers presents a 2:1 ellipse with the axes that vary sinusoidally along its span. Such undulation on the whisker surface can break the spatial coherence of vortex shedding and replace it by complex three-dimensional vortex structures, resulting in a more symmetric pressure distribution on the surface of the whisker, hence substantially decreases the VIV [4,18]. The experiments by Beem and Triantafyllou [5] found that whisker-shaped cylinders experienced very low VIV compare to circular ones under the same Reynolds numbers. When a whisker-shaped cylinder was placed within the wake of a target located upstream, its vibration frequency coincides with the vortex shedding frequency of the upstream target. In such conditions, the whisker-shaped cylinders presented distinct WIV with amplitudes much higher than the VIV cases in the open water environment, even with very large gap distances. This feature enables seals to distinguish the circumstances when they are in the wake flow of upstream targets or just swimming in the open water environment. Following study of Wang and Liu [20] further investigated the wake patterns behind cylinders with various geometries via time-resolved particle velocimetry measurements. They showed that the recirculation regions in the wake of whisker-shaped cylinders is significantly smaller than that of circular cylinders.

As reviewed above, most of the existing works on the mechanisms of WIV and wake-whisker interactions have focused on cases in “fixed-gap,” where the gap distance between the whisker sensor and the upstream target remains constant. In nature, the target of seals (e.g., fishes) may frequently change their swimming status including speed and orientation [21–23]; in such circumstances, the relative positions between seals and upstream targets alter across time, and the associated wake flow impinging on whiskers presents distinctive time-varying patterns. How whisker sensors respond to the unsteady wake flows, and therefore detect the variation of the target’s swimming status, has not been explored in detail. This work aims to contribute to the fundamental understanding of the wake-whisker interaction mechanism with the time-varying gap between the target and the whisker sensor. The schematic of the research concept is shown in Fig. 1, where the target is simplified as a moving cylinder; similar set up can be found in the work of Beem and Triantafyllou [5]. Systematic experiments were conducted to quantify the variation of WIV patterns across time and their linkage to unsteady vortex flow. Meanwhile, theoretical frameworks were implemented to reveal the underlying physics for the variation of the whisker’s sensitivity to the gap growth rate. The results advance our knowledge of how seals track targets with time-varying relative positions, and therefore the improvement of design for bioinspired wake sensors [24–26]. The manuscript is

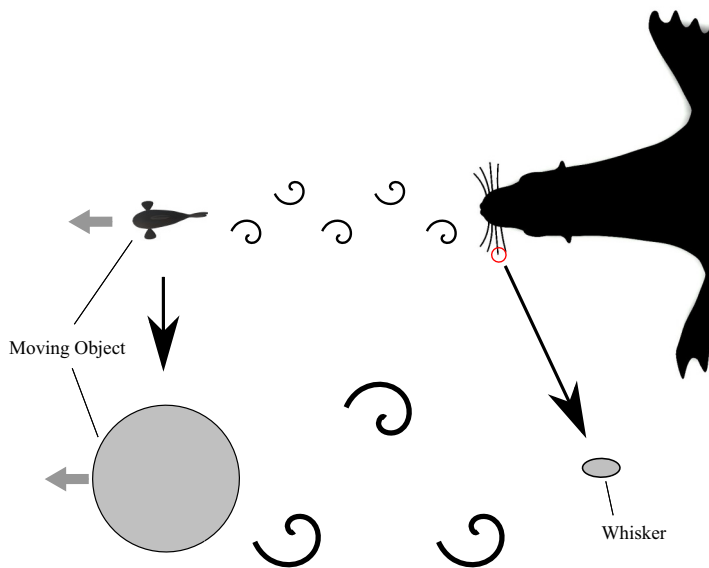


FIG. 1. The analogy between seal whisker sensing and our experimental design.

organized as follows. The experimental setup is illustrated in Sec. II, the results are analyzed in Sec. III, and the main conclusions and remarks are provided in Sec. IV.

II. EXPERIMENTAL SETUP

The experiments were conducted in a recirculation water tunnel in the University of Texas at Dallas. The water tunnel has a test section of 2 m length and 200 mm width with background turbulence level less than 1%. A polylactic acid circular cylinder with diameter $d_c = 35$ mm was vertically mounted on a traversing system, which allowed it to move along the centerline of water channel. The cylinder had a submerged length of $L = 178$ mm and a 2 mm gap between its free-end to the bottom of the water tunnel, which minimized the three-dimensional vortex shedding from the cylinder tip. A 3D printed whisker model with the same submerged length, and a cross-section in the shape of an ellipse with an aspect ratio of 2 was fabricated as the wake sensor in this work. Its axes varied sinusoidally along the whisker, and the wavelength-to-diameter ratio of the whisker was $\lambda/D_w = 2.5$ [see details in Fig. 2(c), where D_w is the hydraulic diameter of whisker]. Such geometry has proven to well suppress the fluid lift produced by the wake flow from the whisker itself with its major axis aligned with water flow [18,27,28]. The averaged spanwise (i.e., in the direction perpendicular to incoming flow) width of the whisker sensor was $d_w = 3.5$ mm, which is one-order-of-magnitude smaller than the size of the circular cylinder to minimize its disturbance to the wake flow. The tip of the whisker was connected to a cantilever spring base, which allowed the whisker to behave as a single-freedom oscillator in the spanwise direction and therefore “sense” the variation of incoming vortex flow. The mass ratio C_m of the vibration system is computed as

$$C_m = \frac{m}{m^*},$$

$$m^* = \rho\pi(2d_w)^2L, \quad (1)$$

where m is the mass of the vibration assembly and m^* is the added mass of the whisker. Based on Eq. (1), the mass ratio in this work was approximately 1.0, which well represents the case for real seal whiskers [5]. The damping coefficient of the system $c = 0.032 \text{ N s m}^{-1}$ was determined by

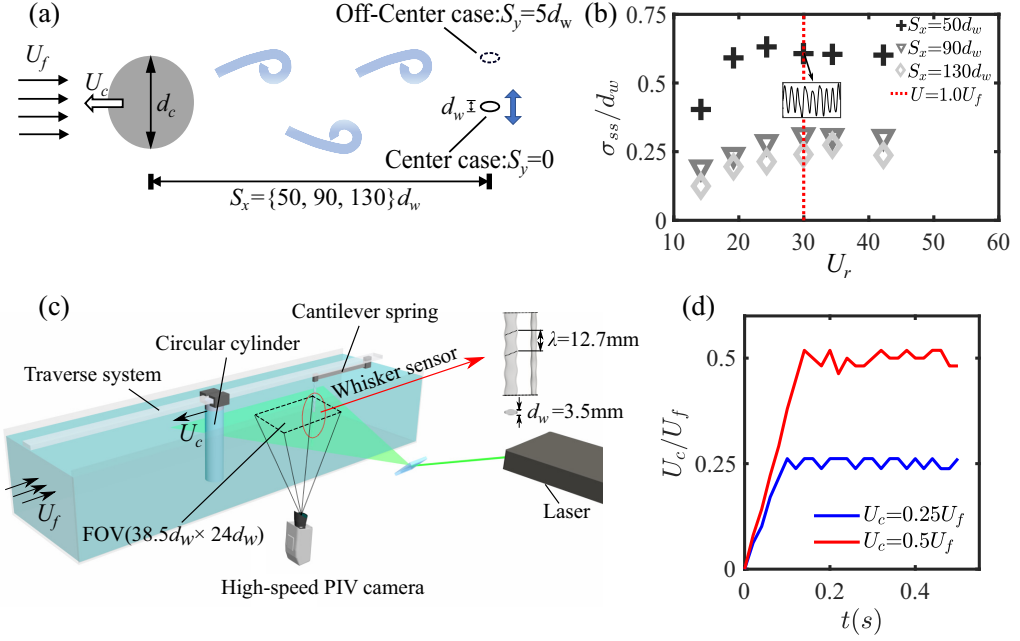


FIG. 2. (a) Layout and top view of the circular cylinder and whisker sensor under flow; (b) the “fixed-gap” WIV intensity of the whisker σ_{ss} under various gap distance S_x and reduced velocity U_r . σ_{ss} is the root-mean-square (RMS) value of the spanwise displacements; (c) schematic of the experimental setup and the geometry of whisker sensor; (d) velocity of the upstream cylinder during the acceleration progress.

free vibration test in the static water, and the same method was adopted in measuring the system’s natural frequency under water with $f_0 = 3.53$ Hz.

The whisker-spring assembly was placed downstream of the circular cylinder in the water channel to allow WIV. At the beginning of each measurement, the circular cylinder was static under the water flow, while the whisker was placed at three initial streamwise gaps $S_x = 50, 90,$ and $130d_w$, and two initial spanwise gap $S_y = 0$ (i.e., wake centerline) and $5d_w$ (i.e., at the edge of circular cylinder) to allow the “fixed-gap” WIV [Fig. 2(a)]. This represents scenarios when the seal and the target are moving in the same speed as explored in previous study [5]. In this work, the incoming flow velocity was fixed at $U_f = 0.37$ m s $^{-1}$, leading to the reduced velocity at $U_r = U_f/(f_0d_w) = 30$ and the Reynolds number at $Re = U_f d_c/\nu = 13\,000$, where ν is the kinematic viscosity of water. It is worth noting that complementary measurement for the “fixed-gap” WIV of the whisker has shown that the vibration intensity σ_{ss}/d_w (σ_{ss} is the standard deviation of whisker displacements during WIV) first increased with U_r within $U_r \leq 30$ and then approached a plateau [Fig. 1(b)]. Therefore, the selected U_r in this work ensures distinctive whisker vibrations under the “fixed-gap” WIV stage. After the WIV of the downstream whisker reached the stable “fixed-gap” vibration for more than 60 s, a signal was sent to the traversing system, and the circular cylinder started to move upstream with different velocities of $U_c \in [0.10, 0.50]U_f$ every $\Delta U_c = 0.05U_f$ until the circular cylinder moved $x_{travel} = 850$ mm away from its initial location. This mimics scenarios when the upstream target change their swimming status with the speeds increasing from U_f to $U_f + U_c$. It is worth noting that as shown in Fig. 2(d), the acceleration time for the upstream cylinder to reach designed U_c is less than 0.135 s, or $0.3T_v$ across all cases. Here $T_v = d_c/(StU_f)$ is the vortex shedding period of the circular cylinder in “fixed-gap” cases, and $St = 0.19$ is the Strouhal number of the circular cylinder measured from this work, which is similar to those reported from previous studies across a wide range of Re [29–31]. Therefore, this acceleration time is ignored when accounting the movement of upstream cylinder in this work.

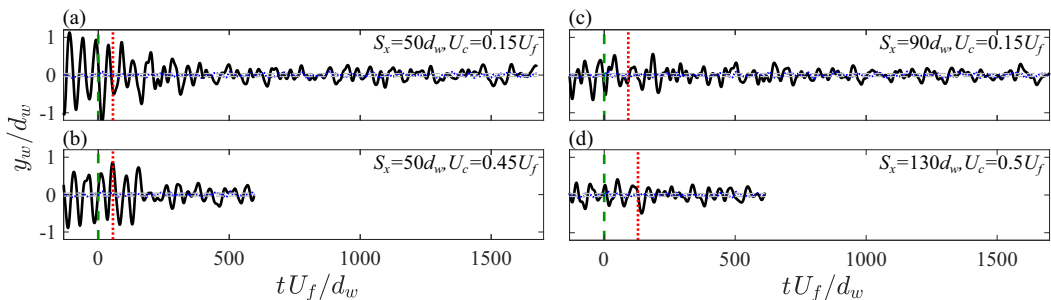


FIG. 3. Time series (black solid lines) of whisker displacements for selected cases. Green vertical lines represent the time when upstream cylinder started to move at $t = 0$. Red vertical lines denote the instant T_{tr} when the induced wake signal reached the whisker sensor. The blue lines denote the time series of whisker displacements in open water flow (i.e., without upstream cylinder) under U_f , and gray dotted lines represent the corresponding $\pm\sigma_{ss}$.

A high-speed, planar particle image velocimetry (PIV) system from TSI was applied to characterize the wake dynamics and WIV response of the whisker sensor. A field of view (FOV) of $135 \text{ mm} \times 84 \text{ mm}$ ($38.5d_w \times 24d_w$) was illuminated via a 1-mm-thick laser sheet from a 30 mJ/pulse laser. The origin of the axis was fixed with the center of the circular cylinder. The water flow was seeded with $14 \mu\text{m}$ silver-coated hollow glass spheres with a density of 1.02 g cm^{-3} . The wake flow and vibrations of the whisker was captured with a 4 MP (2560×1600 pixels), 16-bit CMOS camera at a frequency of 100 Hz. For each case, the PIV measurement was initiated 10s before the movement of the upstream cylinder, and stopped 10s after the circular cylinder reached its terminal location. The instantaneous wake velocities were obtained from the captured image pairs with a recursive cross correlation method via the INSIGHT 4G software from TSI. The interrogation window size was 32 pixels with 50% overlap, leading to a final vector grid spacing of $\Delta x = \Delta y = 0.85 \text{ mm}$. This method ensured vector fields with more than 95% valid vectors on average. Overall, the uncertainty of identified particle locations was approximately 0.1 pixel, leading to $\sim 1.7\%$ uncertainty of velocity measurement considering the bulk particle displacement of ~ 6 pixels between two successive images. To facilitate the tracking of whisker vibrations, a fiducial point was marked at the leading edge of the whisker and illuminated by the laser sheet. The instantaneous whisker displacements were then determined by the geometrical center of the illuminated fiducial point via post-processing from Matlab [32,33]. Based on the resolution of the camera at $50 \mu\text{m}$ per pixel, the uncertainty of whisker displacement is approximately $0.015d_w$.

III. RESULTS AND DISCUSSION

A. Time histories and time-varying WIV amplitudes of whisker sensor

The distinctive impact of time-varying gaps on the WIV of whisker is first reflected via the time-history of its spanwise displacements $y_w(t)$ with selected cases at $S_y = 0$ (i.e., whisker at wake centerline) shown in Fig. 3. Here, $t = 0$ (dashed green line) denotes the moment when the circular cylinder started to move, and a few WIV cycles before the cylinder movement were also included to present the “fixed-gap” WIV stage. For $t \leq 0$, the WIV of the whisker was governed by the periodic vortex shedding from the upstream circular cylinder, where the frequency of vibration well follows the Strouhal relation $f = StU_f/d_c$. The vibration of the whisker presents different patterns soon after the movement of the upstream cylinder. Overall, at the moment of $t = 0$, the amplitude of the whisker WIV remained similar as the “fixed-gap” stage. This is not surprising since the wake signal produced by the cylinder movement requires transport time T_{tr} to reach the whisker. As a first-order approximation, $T_{tr} = S_x/U_{tr}$ (marked with red line) is estimated by the initial gap and the averaged streamwise velocity U_{tr} between the cylinder’s initial location to the whisker. Our

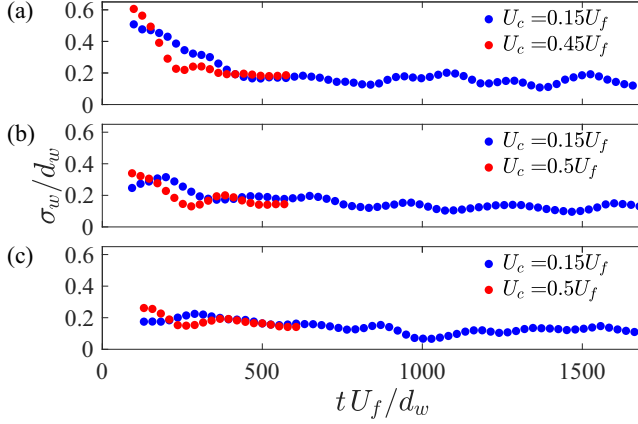


FIG. 4. Time-varying WIV intensity σ_w of the whisker sensor for (a) $S_x = 50d_w$, (b) $S_x = 90d_w$, and (c) $S_x = 130d_w$.

PIV measurements indicate that $U_{tr} = [0.89, 0.97, 0.99]U_f$ for $S_x = [50, 90, 130]d_w$, respectively, which yielded a similar approximation as reported in early studies [34–36]. Afterward (i.e., $t > T_{tr}$), the original whisker vibration pattern was disturbed, where the overall WIV amplitude first exhibited a decrease due to the growth of streamwise gap distance to the upstream cylinder, then approached asymptotically a constant value. It is also worth noting that even when the cylinder had moved 850 mm (i.e., $243 d_w$) away from its initial location, this WIV amplitude was still significantly higher than the case in the open water environment (i.e., VIV of whisker along) under the same U_f shown as the blue lines. This highlighted that the whisker sensor has high “signal-to-noise” ratio and the capability to detect moving targets even with large streamwise gaps.

To further quantify the distinctive time-varying WIV amplitudes due to the movement of the upstream cylinder, the instantaneous WIV intensity is defined as

$$\sigma_w(t) = \sqrt{1/(2T_v) \int_{t-T_v}^{t+T_v} y_w(t)^2 dt}, \quad (2)$$

where $T_v = d_c/(StU_f)$ is the vortex shedding period of the static circular cylinder in flow. Equation (2) calculates the standard deviation of whisker displacements within the neighboring two vortex transport period, which is used to evaluate the time-dependent WIV intensity in this work. Figure 4 illustrates the variation of $\sigma_w(t)$ for representative cases within $t > T_{tr}$ (i.e., after whisker WIV was influenced by gap growth). The results highlight the distinctive coupling between $\sigma_w(t)$, S_x , and U_c of the upstream cylinder. Specifically, for cases with the same S_x , the one with higher U_c resulted in larger WIV intensity right after the cylinder movement. With the growth of time, the case with higher U_c led to more rapid growth of gap and therefore faster reduction of wake fluctuation intensities; this is reflected by the corresponding larger decaying rate of $\sigma_w(t)$ in a short period of time after the movement of circular cylinder. However, the overall decaying rate of WIV intensity is also sensitive to the variation of S_x . Indeed, regardless of U_c , $\sigma_w(t)$ reduced more than 70% when they reach the terminal location with small initial gap at $S_x = 50d_w$. In contrast, this value decreased to approximately 35% when the initial gap increased to $S_x = 130d_w$.

Results discussed above have demonstrated that the decaying rate of WIV intensity of the whisker sensor is modulated by both the gap growth rate to the upstream cylinder and the initial streamwise gap. This quantity can be more clearly reflected via a nondimensional parameter γ_{amp} defined as

$$\gamma_{amp} = \frac{\sigma_w(t \leq 0)/\sigma_w(t = t_{term})}{t_{term}} \frac{d_w}{U_f}, \quad (3)$$

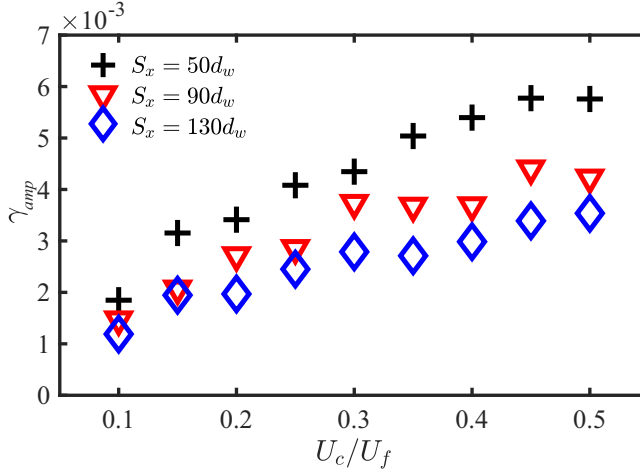


FIG. 5. Decaying rate of WIV intensity over unit time γ_{amp} across various U_c and S_x .

where $\sigma_w(t \leq 0)$ denotes the WIV intensity within “fixed-gap” stage, and $\sigma_w(t = t_{term})$ is the one when the upstream cylinder reached the terminal location at the time t_{term} . The definition of γ_{amp} allows to quantify the variation rate of WIV intensity over a unit time, and therefore the sensitivity of the whisker sensor for detecting the speed change of the upstream cylinder. The distribution of γ_{amp} for all investigated cases is illustrated in Fig. 5. Two trends can be clearly observed from this figure. First, γ_{amp} reduced with the growth of S_x . This corresponds to the observation from Fig. 4 that more rapid decay of WIV occurs with smaller initial gap. Moreover, at a given S_x , although γ_{amp} on the whole increased with U_c and follows our expectation that a faster gap growth rate induces larger WIV intensity decay within a unit time, this trend gradually diminished at higher U_c . Indeed, regardless of S_x , the averaged $\frac{\partial \gamma_{amp}}{\partial (U_c/U_f)}$ within $0.3 \leq U_c/U_f \leq 0.5$ is more than 40% lower compared to that within $0.1 \leq U_c/U_f \leq 0.3$. This result highlighted that the whisker sensor gradually becomes “nonsensitive” for determining the speed change of the upstream cylinder (i.e., U_c) via the decaying rate of WIV intensity when U_c is high. Such phenomenon will be revisited with the discussion of coupling between whisker and wake flow via the physical model in the following sections.

B. On the coupling between whisker WIV and wake dynamics

The coupling of wake flow dynamics and whisker vibrations is illustrated by the distribution of vorticity magnitude and spanwise velocity at representative instants in Figs. 6 and 7. To well illustrate the coupling mechanism, the snapshots were selected based on the vibration cycle when $y_w(t)$ reached local maximum (minimum) displacements and equilibrium locations. First, Fig. 6 presents the WIV of the whisker at “fixed-gap” stage with $S_x = 90d_w$. Here, the incoming vortex A drove the whisker moving toward the negative y -axis direction from its equilibrium location [Fig. 6(a-i)]. The vortex A was accompanied with the approaching of spanwise flow with $v < 0$ [Fig. 6(b-i)], and the associated hydrodynamic loads continually drove the whisker sensor away from equilibrium until it reached the local maximum displacement in the negative y direction. Note that in this instant vortex A just passed the location of the whisker [Fig. 6(a-ii)], while the whisker is still impinged by the spanwise flow toward the negative y -axis direction [Fig. 6(b-ii)]. Despite the spanwise flow load, the restoring force started to drive the whisker back to the positive y -axis direction, where the whisker was within the subsequent vortex structure B when it moves back to the equilibrium location [Fig. 6(a-iii)], and then reached another local maximum displacement accompanied with the spanwise flow toward positive y -axis direction [Figs. 6(a-iv) and 6(b-iv)]. Such coupling between vortex flow and whisker dynamics enabled the periodic WIV in the “fixed-gap”

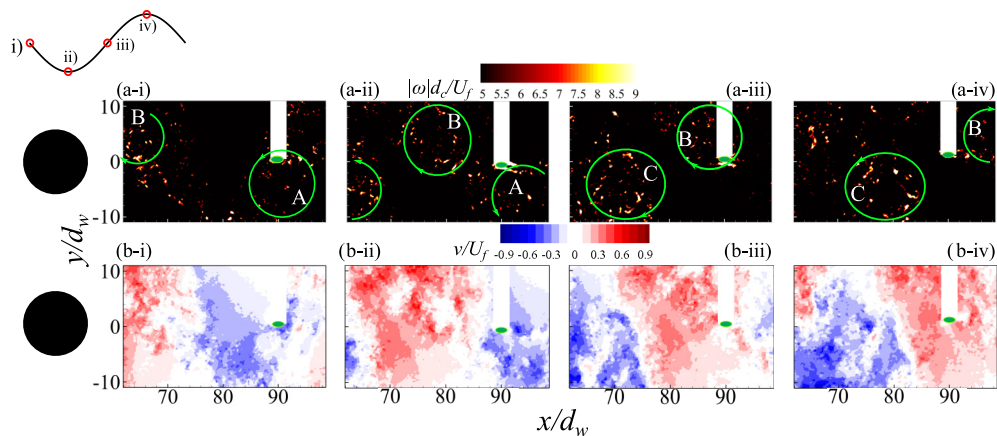


FIG. 6. Selected snapshots of (a) vorticity magnitude and (b) spanwise velocity distributions during one cycle of whisker vibration within “fixed-gap” WIV stage at $S_x = 90d_w$. The instantaneous positions of whisker sensor are superimposed as green ellipses.

stage with similar amplitudes across each cycle, which was also observed for cases with $S_x = 50d_w$ and $130d_w$ not shown here for brief. In contrast to the “fixed-gap” cases, the time-varying gaps due to the movement of the upstream cylinder resulted in significant unsteady vortex strength impinging on the whisker. Figure 7 presents the vortex structure and spanwise flow distributions when the instantaneous gap x_g/d_w increased to approximately 280 with $U_c = 0.2U_f$. Clearly, due to the decaying of vortex strength along downstream distance, both the vortex strength and spanwise flow magnitude exhibited significant reduction compared to those within the “fixed-gap” stage shown in Fig. 6, which corresponded to the decaying WIV amplitudes over time shown in Fig. 4. Meanwhile, for cases with smaller initial gap at $S_x = 50d_w$ and instantaneous gap x_g/d_w increased to approximately 90 (Fig. 8), the produced spanwise flow magnitudes were indeed higher than the corresponding “fixed-gap” scenarios with the same gap observed from Fig. 6. These indicate that the intensities of time-varying hydrodynamic loads impinging on the whisker are determined not only by the instantaneous gaps, but also by the cylinder moving speed. To further explore this evolution, the normalized wake flow circulation is used to quantify the strength of hydrodynamic load, which

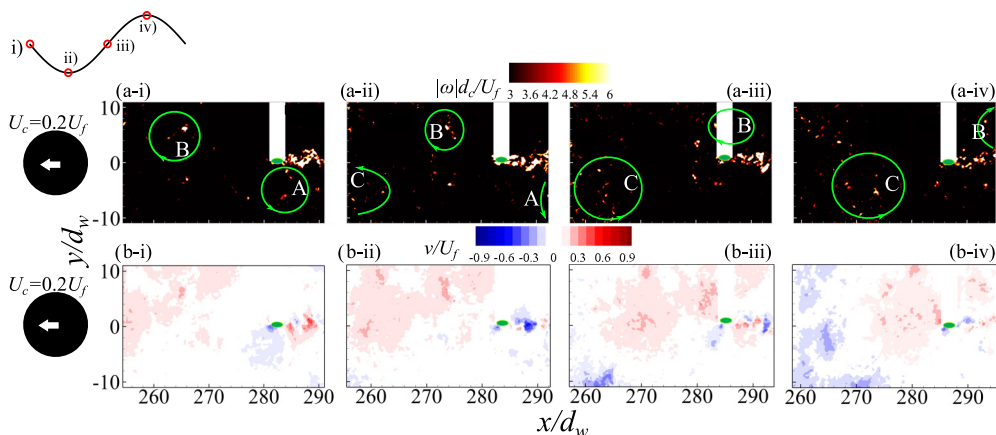


FIG. 7. Same as Fig. 6 but in the moment after cylinder movement with $S_x = 90d_w$, $U_c = 0.2U_f$, and instantaneous gap $x_g/d_w \approx 280$.

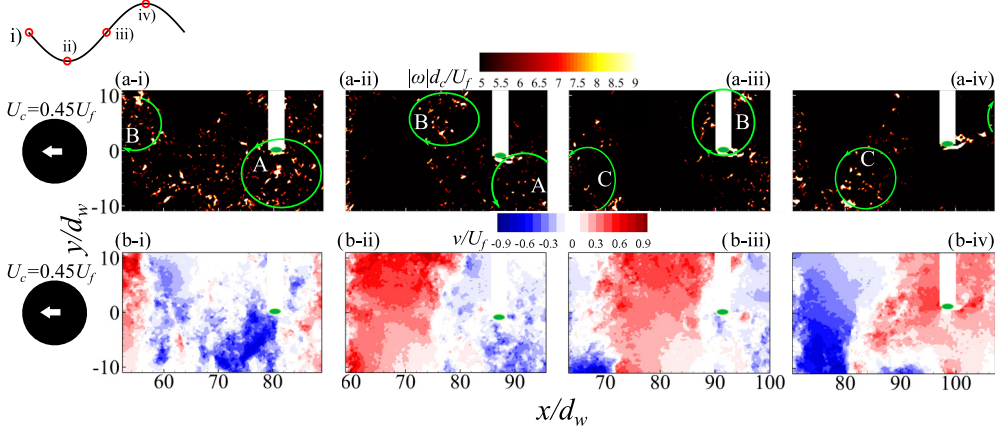


FIG. 8. Same as Fig. 7 but in the moment with $S_x = 50d_w$, $U_c = 0.45U_f$, and $x_g/d_w \approx 90$.

is calculated as

$$\Gamma = \int_A \omega_z dA, \quad (4)$$

where A is integration area within $y < 0$ and the length defined by the averaged streamwise gap between neighboring vortex pairs. Also, we only considered locations where $|\omega_z|d_c/U_f > 0.03$ to minimize the influence of signal noise. The variation of Γ as a function of the instantaneous gap is shown in Fig. 9. The results illustrated that the decaying rate of Γ gradually dropped with the growth of gap x_g/d_w , and cases with higher U_c produced overall stronger Γ at a given instantaneous gap. Further normalization of Γ by the relative speed between the cylinder and surrounding flow $U_c + U_f$ highlighted that regardless of initial gap S_x and cylinder moving speed U_c , the wake circulation strength follows the same decaying trend which behaves as an inversely proportional relation with respect to instantaneous gap x_g/d_c as

$$\frac{\Gamma}{(U_c + U_f)d_c} = \frac{\alpha}{(x_g + x_0)/d_c}, \quad (5)$$

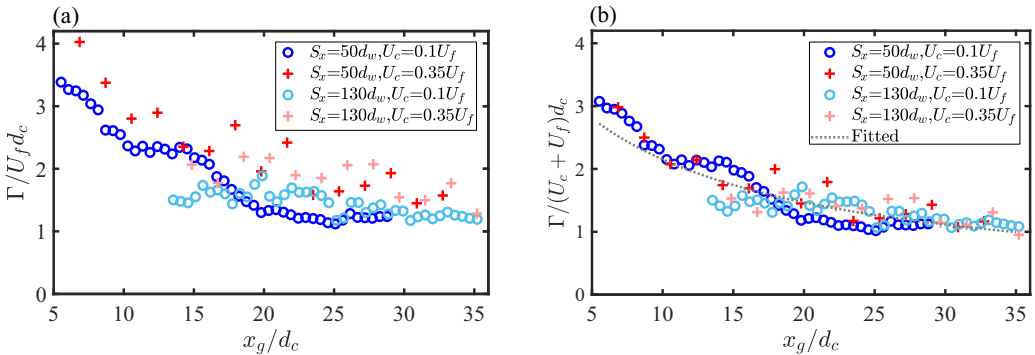


FIG. 9. Distribution of wake circulation strength Γ across instantaneous gaps for selected cases with (a) $S_x = 50d_w$ and (b) $S_x = 130d_w$. Panel (c) summarizes the results from panels (a) and (b) with Γ normalized by $(U_c + U_f)d_c$.

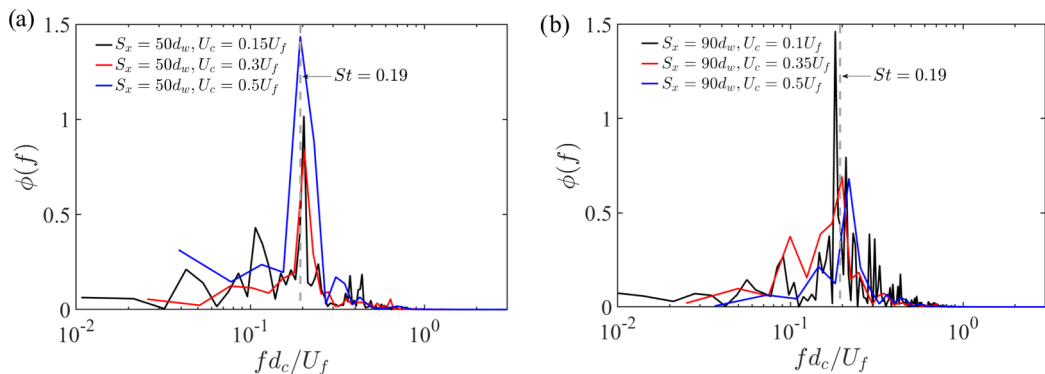


FIG. 10. Spectra of whisker displacements within $t > T_{tr}$ for selected cases with (a) $S_x = 50d_w$ and (b) $S_x = 90d_w$. The gray dashed line denotes the frequency following Strouhal number of $St = 0.19$.

where α and x_0 are constants that are determined by the least square fitting to the experimental data, and the fitted curve is shown in Fig. 9(c) as the gray dotted line. Similar vortex strength decaying trend was also reported by Ponta [36] but at a much lower Reynolds number. Results from Fig. 9 and Eq. (5) illustrate that the higher decaying rate of WIV amplitude with smaller initial gaps observed in Fig. 4 is associated with the more rapid decrease of wake vortex strength in the near wake. Meanwhile, at a given S_x , the larger WIV amplitude at higher U_c right after $t = T_{tr}$ observed in Fig. 4 is attributed to the stronger instantaneous Γ since $\Gamma \propto (U_c + U_f)$, although Γ then also decayed faster as $x_g = U_c t + S_x$.

However, despite the variation of hydrodynamic load strength, the relative phase between whisker displacement and vortex structure (or spanwise velocity distribution) within one cycle illustrated in Figs. 8 and 7 remained overall similar compared to the “fixed-gap” scenario. Indeed, the spectra of whisker displacement after the cylinder movement highlighted that, across all S_x and U_c , the dominating WIV frequency remained at $fd_c/U_f \approx 0.19$ (Fig. 10), i.e., the same as those within the “fixed-gap” stage. Therefore, the WIV of the whisker can be considered as a parametric excitation system, where the external force continually changes the magnitude but remains with the same frequency. This phenomenon can be explained via the vortex transport mechanism by considering an observer moving together with the cylinder at a speed U_c . In such condition, the relative velocity between the cylinder and surrounding water is $U_c + U_f$ with associated vortex shedding frequency as $f_{v,cylinder} = St(U_c + U_f)/d_c$ from the observer. However, the whisker sensor is “retreating” away from the cylinder with a speed of U_c . Therefore, when the vortex signal reached the location of whisker with a transport distance of $S_x + U_c t$ from the cylinder, the frequency of this vortex signal impinging on the whisker presents a “Doppler” effect as $f_{v,whisker} = \frac{U_c + U_f - U_c}{U_c + U_f} f_{v,cylinder} = StU_f/d_c$, which is well supported by our experimental results. It is worth noting that due to the growth of downstream distance, the wake flow may gradually present secondary vortex patterns with different shedding periods [37–40]. The impact of these vortex structures were also reflected in our measurements as secondary peaks of WIV displacement spectra in Fig. 10. Such vortices can bring about disturbance to the synchronization between whisker displacements and evolution of primary vortex, which accounts for the undulations of WIV intensity σ_w across time in far wake regions as exhibited in Fig. 4.

C. Physical modeling for time-dependent WIV

The results discussed in section Sec. 3.2 illustrate that the WIV of the whisker after the cylinder movement remained overall synchronized with incoming vortices, where its time-varying amplitude is modulated by the intensity of hydrodynamic loads influence by both the relative speed between the

upstream cylinder and surrounding water, and the gap growth rate. To further reveal the coupling of both factors on whisker WIV, a physical model based on the balance between time-depending hydrodynamic loads, whisker inertial force, system damping and restoring force is implemented in this section. Here, we start with a few simplifying assumptions. First, we assume that the vortex flow impinging on the whisker sensor can be considered as two-dimensional along the its span, and only the influence of the primary vortex is accounted. Second, the vibration of the whisker sensor has minor disturbance to the incoming vortex structure. Then, as a first-order approximation, the governing equation for WIV of the whisker can be expressed as a harmonic oscillator with decaying external forces:

$$m_t y_w(t)'' + c y_w(t)' + k y_w(t) = 0.5 \rho U_f^2 d_w L C_y(t) \sin(2\pi f_v t), \quad (6)$$

where $y_w(t)$, $y_w(t)'$, and $y_w(t)''$ are the displacement, velocity, and acceleration of the whisker in y -axis direction, respectively, $m_t = m + m^*$ is the mass of whisker vibration system [41], c and k are the damping and stiffness of the vibration system underwater, $C_y(t)$ is the time-varying hydrodynamic force coefficient acting on the whisker in y -axis direction, and $f_v = \text{St}U_f/d_c$ is the frequency of vortices impinging the whisker. Clearly, $C_y(t)$ plays a key role in determining the time-varying WIV amplitude of whisker. To quantify the relation between the hydrodynamic load coefficient and the vortex circulation strength, complementary experiments were conducted with “fixed-gap” WIV of whisker across various gaps x_{ss} downstream of the cylinder under incoming velocity U_f . In such circumstances, C_y no longer changes with time, and the right-hand side of Eq. (6) can be simplified as $0.5 \rho U_f^2 d_w L C_y(x_{ss}) \sin(2\pi f_v t)$, which gives the “fixed-gap” solution of whisker WIV displacement as

$$y_w(t) = A_{ss} \sin(2\pi f_v t + \varphi),$$

$$A_{ss} = \frac{0.5 \rho U_f^2 d_w L C_y(x_{ss})}{k \left\{ \left(1 - \frac{f_v^2}{f_0^2}\right)^2 + \left(2\zeta \frac{f_v}{f_0}\right)^2 \right\}^{\frac{1}{2}}}, \quad (7)$$

where A_{ss} denotes the “fixed-gap” vibration amplitude of the whisker, φ is the phase angle, and $\zeta = 0.5c/(k/m)^{0.5}$ is the damping ratio. Equation (7) allows to quantify the hydrodynamic load coefficient C_y based on the measured A_{ss} across various gaps as

$$C_y(x_{ss}) = \frac{k A_{ss} \left\{ \left(1 - \frac{f_v^2}{f_0^2}\right)^2 + \left(2\zeta \frac{f_v}{f_0}\right)^2 \right\}^{\frac{1}{2}}}{\frac{1}{2} \rho U_f^2 d_w L}. \quad (8)$$

However, the wake vortex circulation strength downstream of the circular cylinder under incoming flow velocity U_f at a given gap x_{ss} can be calculated following Eq. (5) as $\Gamma(x_{ss}) = \alpha U_f d_c^2 / (x_{ss} + x_0)$. Results for the evolution of both $C_y(x_{ss})$ and $\Gamma(x_{ss})$ as a function of x_{ss} under “fixed-gap” WIV are summarized in Fig. 11. Here, although both parameters decreased with x_{ss} as expected, $C_y(x_{ss})$ exhibited a more rapid decaying trend. Indeed, considering that hydrodynamic loads are proportional to the square of effective velocity impinging on objects and vorticity magnitude is proportional to wake velocity shear, $C_y(x_{ss})$ is expected to behave as $C_y(x_{ss}) \propto \Gamma^2(x_{ss})$. This trend is verified in the subplot of Fig. 11, where the least square fitting indicates that $C_y = \beta \left(\frac{\Gamma}{U_f d_c}\right)^2$ with $\beta = 0.042$. Then, by substituting this expression and Eqs. (5) to (6), the WIV of whisker can be determined as

$$m_t y_w(t)'' + c y_w(t)' + k y_w(t) = 0.5 \rho U_f^2 d_w L \beta \left[\frac{\alpha (U_c + U_f) d_c}{(S_x + U_c t + x_0) U_f} \right]^2 \sin(2\pi f_v t). \quad (9)$$

The time series of whisker WIV predicted by Eq. (9) with comparison to the measured ones are illustrated in Fig. 12 for selected cases. Note that the initial condition of Eq. (9) is adopted from experimental data including $y_w(t = T_{tr})$ and $y_w'(t = T_{tr})$. Overall, the physical model shows good agreement with the experimental results, especially for the overall decaying rate of WIV intensity

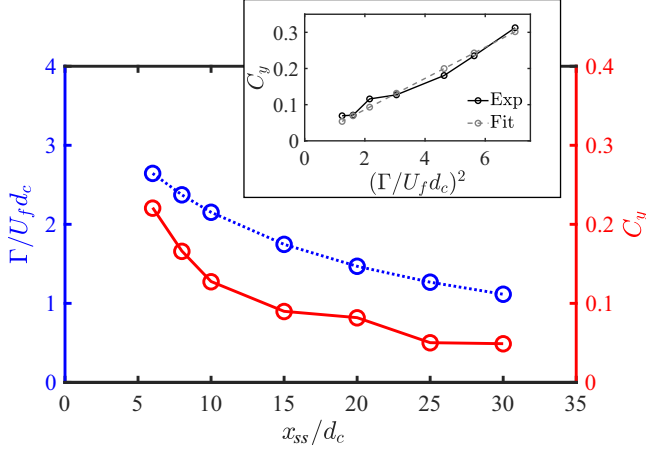


FIG. 11. Distribution of wake circulation strength Γ and the associated hydrodynamic force coefficient C_y as a function of streamwise gap x_{ss} measured from “fixed-gap” WIV. Subplot reveals the relations between Γ and C_y which follows $C_y \propto \Gamma^2$.

with time across various S_x and U_c ; the slight mismatching of y_w especially in the far wake region can be attributed to the impact of secondary vortex structures, which is not included in the current model. Moreover, this model allows explaining the reduced sensitivity of whisker sensor when U_c is sufficiently high as observed in Fig. 5. Indeed, based on Eq. (9), the normalized decaying rate of hydrodynamic load intensities over a unit time can be expressed as

$$\begin{aligned} \gamma_{\text{load}} &= \frac{C_y(t \leq 0)/C_y(t = t_{\text{term}})}{t_{\text{term}}} \frac{d_w}{U_f} = \frac{\left(\frac{\alpha U_f d_c^2}{S_x + x_0} / \frac{\alpha (U_c + U_f) d_c^2}{S_x + x_{\text{travel}} + x_0}\right)^2}{x_{\text{travel}}/U_c} \frac{d_w}{U_f} \\ &= \frac{U_f U_c}{(U_c + U_f)^2} \left(\frac{S_x + x_{\text{travel}} + x_0}{S_x + x_0}\right)^2 \frac{d_w}{x_{\text{travel}}}. \end{aligned} \quad (10)$$

The variation of γ_{load} (dashed lines) across various S_x and U_c predicted by Eq. (10) is superimposed with the decaying rate of WIV intensity γ_{amp} in Fig. 13; overall, these two parameters present very similar trends. Equation (10) highlights that for upstream cylinder moving from the same initial gap

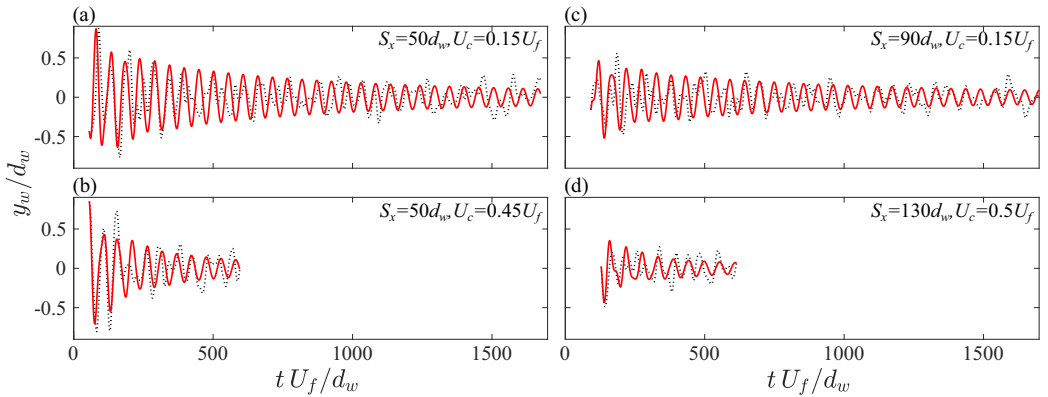


FIG. 12. Measured (black dashed lines) and modeled (red solid lines) time series of whisker displacements for selected cases.

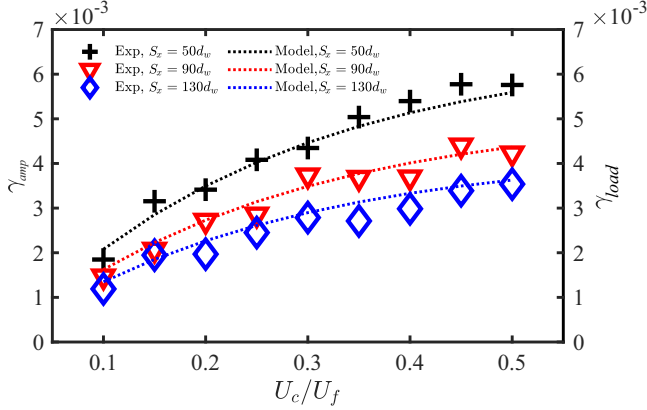


FIG. 13. The distribution of modeled hydrodynamic load decaying rate γ_{load} superimposed with measured γ_{amp} across various S_x and U_c .

S_x , only the term $\frac{U_f U_c}{(U_c + U_f)^2}$ determines the decaying rate of hydrodynamic loads acting on whisker sensor. In particular, when $U_c \ll U_f$, $\frac{U_f U_c}{(U_c + U_f)^2}$ (and therefore γ_{load}) increases almost linearly with U_c . In such conditions, γ_{load} is sensitive to U_c , where the decaying rate of hydrodynamic loads is dominated by the gap growth rate between the upstream target and the whisker. However, $\frac{\partial \gamma_{load}}{\partial U_c}$ gradually decreases with the growth of U_c , where higher U_c resulted in stronger vortices produced by the moving cylinder and therefore hydrodynamic loads acting on the whisker sensor, which compensated the influence of gap growing rate.

D. Effect of spanwise gap

The discussions above for the coupling between time-varying incoming vortex flow and whisker response have revealed the distinctive impact of streamwise gap distance and gap growth rate on the WIV patterns. In this section, complementary measurements were performed to investigate the effect of spanwise gap on whisker sensing. Here, the spanwise position of the whisker-spring system in static water shifted from the wake centerline to the cylinder edge, while all other experimental conditions remained the same. Figure 14 shows the representative time-series of whisker displacement. Although the peak-to-peak amplitude of WIV also presented gradual decay trend after the movement of the upstream cylinder, the equilibrium vibration position during each cycle was continually shifting with time. Specifically, before the movement of the upstream cylinder (i.e.,

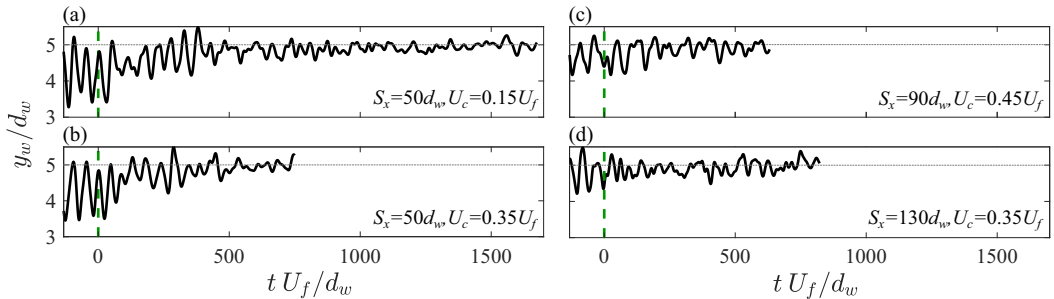


FIG. 14. Time series of whisker displacements for selected cases with $S_y = 5d_w$. The gray dot line denotes the equilibrium position of whisker sensor in static water.

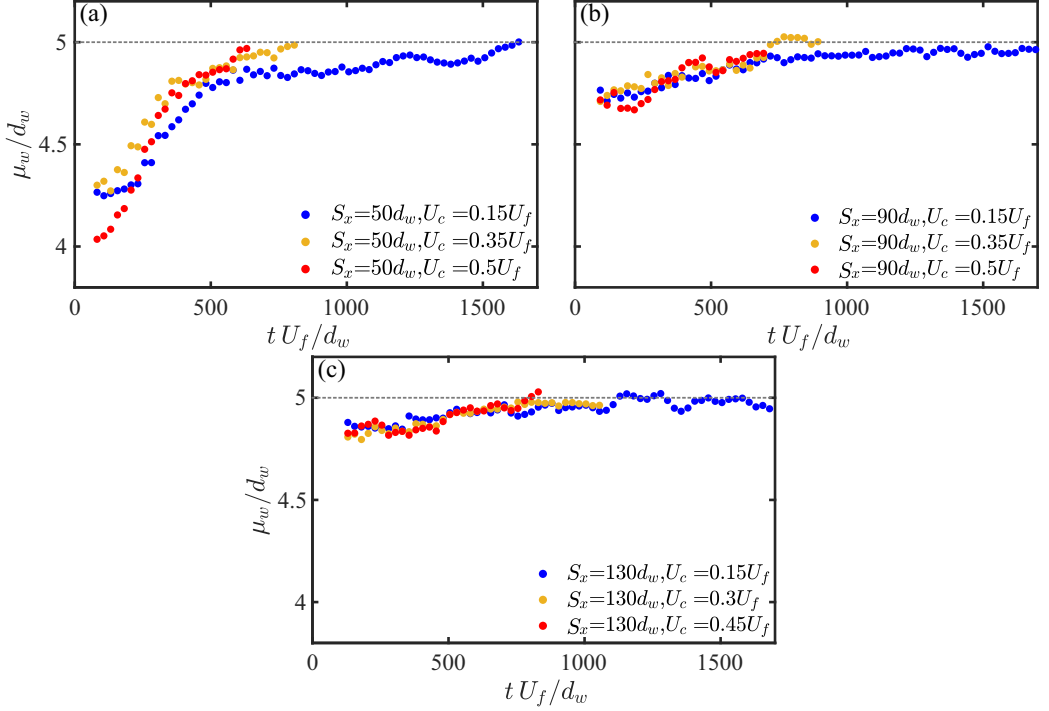


FIG. 15. Time series of equilibrium whisker vibration positions μ_w for selected cases with (a) $S_x = 50d_w$; (b) $S_x = 90d_w$; (c) $S_x = 130d_w$. The horizontal gray dashed line denotes the equilibrium position in static water.

$t \leq 0$), the equilibrium vibration positions were all shifted toward the wake centerline, especially for cases with small streamwise gap at $S_x = 50d_w$ [Figs. 14(a) and 14(b)]. The growth of the streamwise gap after the cylinder movement gradually brought the equilibrium WIV position back to the cylinder edge (horizontal dashed line in Fig. 14). This trend is more clearly reflected by the time series of equilibrium vibration position $\mu_w(t)$ for selected cases shown in Fig. 15. Similar to the definition of σ_w , $\mu_w(t)$ was calculated by averaging the whisker displacement within two vibration cycles as

$$\mu_w(t) = 1/(2T_v) \int_{t-T_v}^{t+T_v} y_w(t) dt. \quad (11)$$

Results in Fig. 15 highlighted that the maximum shifting of equilibrium WIV position, i.e., $5d_w - \mu_w(t)$, can reach up to d_w at $S_x = 50d_w$ and $U_c = 0.5U_f$ when cylinder just started to move. Note that this shifting magnitude is already comparable to the standard deviation of WIV displacement shown in Fig. 14, indicating that for whisker not located in the wake centerline, the variation of its equilibrium WIV position can also be used as a parameter for sensing the time-varying gaps to upstream target. Indeed, this phenomenon can be attributed to the “wake-stiffness” effect as reported by Assi *et al.* [42], where the lower pressure at the wake centerline compared to the edge regions acted as a spring and modulated the whisker vibration positions [43]. Such “wake-stiffness” effect gradually decreases with the growth of downstream distance to the cylinder due to the smaller spanwise pressure gradient.

Finally, the decaying rate of WIV intensity was calculated following Eq. (3) and shown in Fig. 16. To facilitate the comparison, γ_{amp} for whiskers in the wake center were also included. Overall, the distribution of γ_{amp} presented a very similar trend for the whisker in both wake center and cylinder

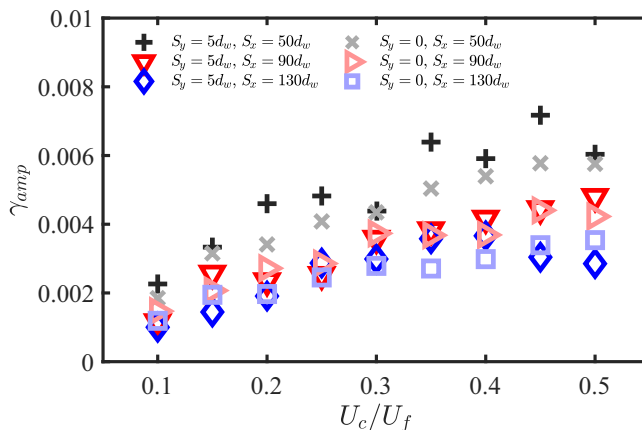


FIG. 16. Decaying rate of whisker vibration intensity γ_{amp} at both $S_y = 0$ and $S_x = 5d_w$.

edge. Further investigation for the time-averaged wake flow vorticity magnitude in Fig. 17 revealed that, the distribution of averaged vorticity magnitude $|\omega|$ along streamwise direction exhibited minor difference across the spanwise locations within $y/d_c \in [-0.5, 0.5]$. These results highlight that the combination of WIV intensities and equilibrium positions is required for the whisker sensor to detect its relative locations to the upstream cylinder in both streamwise and spanwise directions.

IV. CONCLUSION AND REMARKS

In summary, our integrated experimental campaigns and physical modeling revealed the fluid-structure interaction mechanisms of the whisker sensor with time-varying gaps to an upstream cylinder. Overall, with the linearly increasing gap between the cylinder and whisker sensor, the wake-induced vibrations (WIV) of the whisker remained synchronized with the incoming vortex flow, whereas the vibration amplitudes gradually decayed over time. We demonstrated that the decaying rate of whisker vibration intensities over a unit time was higher with smaller initial gaps. Moreover, although a more distinctive decay of WIV intensity occurred with faster growth of the gap, this trend gradually diminished when the gap growth rate became sufficiently high. This is attributed to the stronger vortices and associated hydrodynamic loads in the wake flow initiated by the faster movement of upstream cylinder, which compensated for the influence of the gap

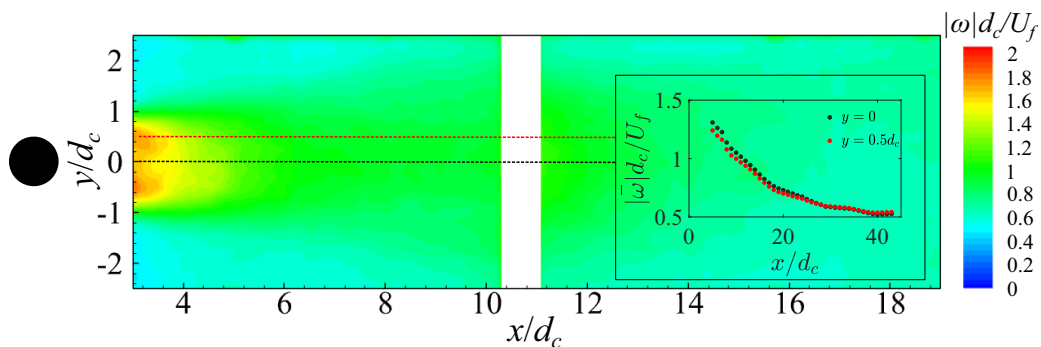


FIG. 17. Normalized vorticity magnitude distribution in the cylinder wake; the subplot shows extracted vorticity magnitude profile along streamwise distance at $y = 0$ (black) and $y = 0.5d_c$ (red).

growing rate. Such decaying of WIV amplitudes across various initial gaps and gap growth rates was well described via a physical model based on the balance between whisker inertial force, system damping, whisker stiffness, and time-varying hydrodynamic loads. Our complementary measurements for whisker sensor at different spanwise locations in the wake flow revealed that, the “wake-stiffness” effect allowed to alter the equilibrium WIV positions, whereas the decaying rate of WIV amplitudes was nonsensitive to the variation of spanwise locations.

In this work, we have taken a step to quantitatively assess the response and sensitivity of the whisker when the upstream target alters its swimming status. The results advance our understanding for the underlying physics of how aquatic animals, such as seals, track complex movements of their targets via wake-induced vibrations of their flow sensors. It is worth pointing out that in this work, we have explored cases with linearly increasing gaps between the whisker and target along streamwise direction. In realistic aquatic environments, the relative positions between the upstream target and the downstream tracker may vary nonlinearly across time in three-dimensional domain [44,45]. In such scenarios, the vortex shedding frequency and strength and associated wake-whisker interaction mechanism are expected to exhibit more complex patterns, which deserve close inspection in future studies.

ACKNOWLEDGMENT

This work was supported by the Department of Mechanical Engineering, The University of Texas at Dallas, as part of the start-up package of Dr. Yaqing Jin. The authors report no conflict of interest.

-
- [1] G. Dehnhardt, B. Mauck, W. Hanke, and H. Bleckmann, Hydrodynamic trail-following in harbor seals (*Phoca vitulina*), *Science* **293**, 102 (2001).
 - [2] N. Schulte-Pelkum, S. Wieskotten, W. Hanke, G. Dehnhardt, and B. Mauck, Tracking of biogenic hydrodynamic trails in harbor seals (*Phoca vitulina*), *J. Expl Biol.* **210**, 781 (2007).
 - [3] K. C. Catania, J. F. Hare, and K. L. Campbell, Water shrews detect movement, shape, and smell to find prey underwater, *Proc. Natl. Acad. Sci. USA* **105**, 571 (2008).
 - [4] F. E. Fish, L. E. Howle, and M. M. Murray, Hydrodynamic flow control in marine mammals, *Integr. Comp. Biol.* **48**, 788 (2008).
 - [5] H. R. Beem and M. S. Triantafyllou, Wake-induced “slaloming” response explains exquisite sensitivity of seal whisker-like sensors, *J. Fluid Mech.* **783**, 306 (2015).
 - [6] C. H. K. Williamson and R. Govardhan, Vortex-induced vibrations, *Annu. Rev. Fluid Mech.* **36**, 413 (2004).
 - [7] M. M. Zdravkovich, Review of flow interference between two circular cylinders in various arrangements, *ASME J. Fluids Eng.* **99**, 618 (1977).
 - [8] T. Igarashi, Characteristics of the flow around two circular cylinders arranged in tandem: First report, *Bull. JSME* **24**, 323 (1981).
 - [9] D. Sumner, Two circular cylinders in cross-flow: A review, *J. Fluids Struct.* **26**, 849 (2010).
 - [10] A. Bokaian and F. Geoola, Wake-induced galloping of two interfering circular cylinders, *J. Fluid Mech.* **146**, 383 (1984).
 - [11] M. M. Zdravkovich, Review of interference-induced oscillations in flow past two parallel circular cylinders in various arrangements, *J. Wind Eng. Ind. Aerodyn.* **28**, 183 (1988).
 - [12] G. R. S. Assi, P. W. Bearman, and J. R. Meneghini, On the wake-induced vibration of tandem circular cylinders: The vortex interaction excitation mechanism, *J. Fluid Mech.* **661**, 365 (2010).
 - [13] D. Brika and A. Laneville, The flow interaction between a stationary cylinder and a downstream flexible cylinder, *J. Fluids Struct.* **13**, 579 (1999).
 - [14] F. J. Huera-Huarte and P. W. Bearman, Vortex and wake-induced vibrations of a tandem arrangement of two flexible circular cylinders with near wake interference, *J. Fluids Struct.* **27**, 193 (2011).

- [15] F. J. Huera-Huarte and M. Gharib, Vortex-and wake-induced vibrations of a tandem arrangement of two flexible circular cylinders with far wake interference, *J. Fluids Struct.* **27**, 824 (2011).
- [16] G. R. S. Assi, Wake-induced vibration of tandem cylinders of different diameters, *J. Fluids Struct.* **50**, 329 (2014).
- [17] F. S. Hover and M. S. Triantafyllou, Galloping response of a cylinder with upstream wake interference, *J. Fluids Struct.* **15**, 503 (2001).
- [18] W. Hanke, M. Witte, L. Miersch, M. Brede, J. Oeffner, M. Michael, and G. Dehnhardt, Harbor seal vibrissa morphology suppresses vortex-induced vibrations, *J. Expl Biol.* **213**, 2665 (2010).
- [19] C. C. Ginter, T. J. DeWitt, F. E. Fish, and C. D. Marshall, Fused traditional and geometric morphometrics demonstrate pinniped whisker diversity, *PLoS ONE* **7**, e34481 (2012).
- [20] S. Wang and Y. Liu, Wake dynamics behind a seal-vibrissa-shaped cylinder: A comparative study by time-resolved particle velocimetry measurements, *Exp. Fluids* **57**, 32 (2016).
- [21] E. D. Tytell, Kinematics and hydrodynamics of linear acceleration in eels, *Anguilla rostrata*, *Proc. R. Soc. Lond. B* **271**, 2535 (2004).
- [22] Z. Ren, V. Di Santo, K. Hu, T. Yuan, T. Wang, L. Wen, and G. V. Lauder, Understanding fish linear acceleration using an undulatory biorobotic model with soft fluidic elastomer actuated morphing median fins, *Soft Robot.* **5**, 375 (2018).
- [23] S. Podila and Y. Zhu, Animating predator and prey fish interactions, *Comput. Anim. Virtual Worlds* **30**, e1866 (2019).
- [24] P. V. Y. Alvarado, V. Subramaniam, and M. Triantafyllou, Design of a bio-inspired whisker sensor for underwater applications, in *Proceedings of SENSORS 2012* (IEEE, Piscataway, NJ, 2012), pp. 1–4.
- [25] H. Beem, M. Hildner, and M. Triantafyllou, Calibration and validation of a harbor seal whisker-inspired flow sensor, *Smart Mater. Struct.* **22**, 014012 (2013).
- [26] W. C. Eberhardt, B. F. Wakefield, C. T. Murphy, C. Casey, Y. Shakhsheer, B. H. Calhoun, and C. Reichmuth, Development of an artificial sensor for hydrodynamic detection inspired by a seal’s whisker array, *Bioinspir. Biomim.* **11**, 056011 (2016).
- [27] H. Beem, Y. Liu, G. Barbastathis, and M. Triantafyllou, Vortex-induced vibration measurements of seal whiskers using digital holography, in *Proceedings of OCEANS 2014 - TAIPEI* (IEEE, Piscataway, NJ, 2014), pp. 1–4.
- [28] A. G. P. Kottapalli, M. Asadnia, J. M. Miao, and M. S. Triantafyllou, Harbor seal whisker inspired flow sensors to reduce vortex-induced vibrations, in *Proceedings of the 28th IEEE International Conference on Micro Electro Mechanical Systems (MEMS’15)* (IEEE, Piscataway, NJ, 2015), pp. 889–892.
- [29] G. S. West and C. J. Apelt, The effects of tunnel blockage and aspect ratio on the mean flow past a circular cylinder with Reynolds numbers between 10^4 and 10^5 , *J. Fluid Mech.* **114**, 361 (1982).
- [30] M. König, U. Fey, and H. Eckelmann, A new Strouhal-Reynolds number relationship for the circular cylinder in the range $47 < Re < 2 \times 10^5$, *Phys. Fluids* **10**, 1547 (1998).
- [31] G. R. Assi and P. W. Bearman, Vortex-induced vibration of a wavy elliptic cylinder, *J. Fluids Struct.* **80**, 1 (2018).
- [32] Y. Jin, J. T. Kim, Z. Mao, and L. P. Chamorro, On the couple dynamics of wall-mounted flexible plates in tandem, *J. Fluid Mech.* **852**, R2 (2018).
- [33] Y. Jin, J.-T. Kim, S. Cheng, O. Barry, and L. P. Chamorro, On the distinct drag, reconfiguration and wake of perforated structures, *J. Fluid Mech.* **890**, A1 (2020).
- [34] M. S. Bloor and J. H. Gerrard, Measurements on turbulent vortices in a cylinder wake, *Proc. R. Soc. Lond. Series A: Math. Phys.* **294**, 319 (1966).
- [35] Y. Zhou and R. A. Antonia, Convection velocity measurements in a cylinder wake, *Exp. Fluids* **13**, 63 (1992).
- [36] F. L. Ponta, Vortex decay in the Kármán eddy street, *Phys. Fluids* **22**, 093601 (2010).
- [37] H. M. Nagib, J. M. Cimbalá, and A. Roshko, Large structure in the far wakes of two-dimensional bluff bodies, *J. Fluid Mech.* **190**, 265 (1988).
- [38] D. Georgiev, P. Vorobieff, and M. S. Ingber, Onset of the second wake: Dependence on the Reynolds number, *Phys. Fluids* **14**, L53 (2002).
- [39] B. Kumar and S. Mittal, On the origin of the secondary vortex street, *J. Fluid Mech.* **711**, 641 (2012).

- [40] H. Jiang and L. Cheng, Transition to the secondary vortex street in the wake of a circular cylinder, *J. Fluid Mech.* **867**, 691 (2019).
- [41] C. E. Brennen, A review of added mass and fluid inertial forces, Technical Report DTIC Document (Sierra Madre, California, 1982).
- [42] G. R. D. S. Assi, P. W. Bearman, B. S. Carmo, J. R. Meneghini, S. J. Sherwin, and R. H. J. Willden, The role of wake stiffness on the wake-induced vibration of the downstream cylinder of a tandem pair, *J. Fluid Mech.* **718**, 210 (2013).
- [43] J. McClure and S. Yarusevych, Surface and wake pressure fluctuations of a cylinder in transitional flow regime, in *Proceedings of the 18th International Symposium on the Application of Laser and Imaging Techniques to Fluid Mechanics* (Lisbon, Portugal, 2016), pp. 4–7.
- [44] P. Domenici, The scaling of locomotor performance in predator-prey encounters: From fish to killer whales, *Comp. Biochem. Phys. A* **131**, 169 (2001).
- [45] P. Domenici, Escape trajectory, Wiley StatsRef: Statistics Reference Online (2014), <https://www.wiley.com/learn/wileystatsref/>.